ELSEVIER

Journal of Hydrology 251 (2001) 186–201

Journal of Hydrology

www.elsevier.com/locate/jhydrol

Using microscope observations of thin sections to estimate soil permeability with the Kozeny–Carman equation

Marcel G. Schaap*, Inma Lebron

George E. Brown Jr. US Salinity Laboratory, USDA-ARS, 450 W. Big Springs Road, Riverside, CA 92507, USA

Abstract

In this study we used the Kozeny–Carman (K–C) equation as a semi-physical model for estimating the soil permeability using data derived from microscope observations. Specific surface areas and porosities were obtained from two-point correlation functions derived from scanning electron microscope images of thin sections using a magnification of 50 and a resolution of 1.88 μm pixel^{-1}. Permeabilities were predicted using two published ('Ahuja' and 'Berryman') and one generalized variant of the K–C equation. The latter model was similar to the Berryman variant, but used a free parameter C rather than a porosity dependent formation factor. All K–C model variants were optimized on measured permeabilities. The Ahuja and Berryman K–C models performed relatively poorly with R^2 values of 0.36 and 0.57, respectively, while the generalized model attained R^2 values of 0.91. The parameter C was strongly related to texture and, to a lesser extent, particle density. The general model still required measured surface area and porosity. However, we showed that it was possible to estimate these parameters from texture resulting in an R^2 of 0.87. A fully empirical model that did not assume K–C concepts performed slightly worse ($R^2 = 0.84$). The results indicate that after developing the model using microscope information, only macroscopic data are necessary to predict permeability of soils in a semi-physical manner with the K–C equation.

Keywords: Soils; Conductivity; Permeability; Thin sections; Correlation; Microscopic methods

1. Introduction

Various techniques are presently available to estimate saturated and unsaturated soil hydraulic properties from surrogate data. Known as pedotransfer functions, these methods commonly predict the hydraulic properties from macroscopic parameters such as texture and bulk density. Most pedotransfer functions are empirical and do not give much insight into the physical relations among soil properties.

A limited number of pedotransfer functions exist that have some physical basis. For example, the models by Haverkamp and Parlange (1986), Arya and Paris (1981), and Arya et al. (1999a,b) derive the water retention or hydraulic conductivity characteristics through shape similarities between pore and particle distributions. Mualem (1976), among others, developed a pore-size distribution model to infer the unsaturated hydraulic conductivity from the water retention characteristic. Most physical models are based on simple capillary tube representations of porous media. Tuller et al. (1999) and Or and Tuller (1999, 2000) recently developed a more realistic model for pore space geometry by describing the porous medium in terms of angular and slit-shaped pores. This model accounts for both adsorptive and capillary forces and accurately described retention and flow through fractured media. Because fluid

* Corresponding author. Tel.: +1-909-369-4844; fax: +1-909-342-4964.

E-mail address: mschaap@ussl.ars.usda.gov (M.G. Schaap).

0022-1694/01/$ - see front matter
PII: S0022-1694(01)00468-1

Nomenclature

List of symbols and abbreviations

β	void ratio
ϕ	total porosity
ϕ_e	effective porosity
ϕ_a	apparent porosity
η	dynamic viscosity (kg m^{-1} s^{-1})
ρ	fluid density (kg m^{-3})
τ	tortuosity
c	geometry factor in Eq. (6)
h	resolution (μm pixel^{-1})
k	permeability (m^2)
m	exponent in Eq. (8)
r	one-dimensional correlation distance (μm)
s	specific surface area (μm^{-1})
u	horizontal lag distance in correlation function (pixels)
v	vertical lag distance in correlation function (pixels)
x	horizontal distance in SEM image (pixels)
x_{max}	maximum horizontal distance in SEM image (pixels)
y	vertical distance in SEM image (pixels)
y_{max}	maximum vertical distance in SEM image (pixels)
A	fitting parameter in Eq. (5) (m^2)
B	fitting parameter in Eq. (5)
C	lumped parameter in Eq. (9)
F	formation factor in Eq. (7)
G	pore geometry factor
K_s	saturated hydraulic conductivity (m s^{-1})
N	number of samples
R_{hv}	hydraulic radius of the void space (μm)
R_{hs}	hydraulic radius of the particle space (μm)
R_c	characteristic pore size, Eq. (21) (μm)
R_L	long-range correlation distance (μm)
$R_z(r)$	one-imensional correlation function
$R_z(u,v)$	two-dimensional correlation function
$R_{z,n}(u,v)$	normalized two-dimensional correlation function
SEM	scanning electron microscope
TPCF	two-point correlation function
$Z(x,y)$	SEM image
RMSE	root mean square error

flow and retention are essentially microscale processes, all physically based models must rely on microscopic relations among pores, particles, and/or surface areas. However, few models use direct observations at the microscale because measurements are generally impractical, difficult, expensive, or even impossible. Instead, they rely on macroscopic proxies to parameterize microscale phenomena.

Microscope observations of thin sections of soils and rocks are the traditional domain of micromorphologists. Observations often result in qualitative data about pedological properties and processes, although quantitative measurements have also been performed (e.g. Bouma et al., 1979). Vogel (1997) used microscope observations of serial thin sections to establish the three-dimensional pore distribution and -connectivity of two soils. Using the same technique supplemented with pore-network modeling, Vogel and Roth (1998) derived hydraulic characteristics and compared these to measured unsaturated conductivities. Quiblier (1984) and Berryman and Blair (1987) used digitized images of thin sections of sand- and limestone to predict permeability. Both studies used the images to derive two-point correlation functions (TPCFs), which provide the spatial correlation structure of the pore space. Berryman and Blair (1987) and Blair et al. (1996) subsequently calculated specific surface area and porosity from the TPCFs and used these to predict permeability with the Kozeny–Carman (K–C) equation. Quiblier (1984) and Adler et al. (1992) used TPCFs in conjunction with numerical simulations of flow at the pore-scale using the Navier–Stokes equation.

The goal of this study is to investigate whether the K–C (Carman, 1939) equation can be used as a physically based model to predict the permeability of soils. The original definition of the K–C equation is somewhat impractical because it requires data such as pore geometry, pore tortuosity, porosity, and specific surface area. We will test two K–C variants that make simplifying assumptions using one (Berryman and Blair, 1987) or two (Ahuja et al., 1984) adjustable parameters. A third more general K–C variant has one adjustable parameter that we will relate to microscopically

derived predictors, macroscopic predictors (texture, soil density), or both. The microscopic variables used for the K–C equation will be derived from TPCFs of scanning electron microscope (SEM) images of thin sections. Because such microscale variables are difficult to observe, we will also develop a model that estimates the microscopic K–C parameters from macroscopic predictors. This model will be compared with a fully empirical model that does not use the K–C concepts but estimates the permeability directly from macroscopic predictors.

2. Theory

2.1. The Kozeny–Carman equation

The saturated hydraulic conductivity, K_s (ms^{-1}), is determined by porous medium as well as the fluid properties

$$K_s = \frac{\rho g}{\eta} k \tag{1}$$

where ρ is the fluid density ($kg\ m^{-3}$), g is acceleration of gravity ($m\ s^{-2}$), and η the dynamic viscosity of the fluid ($kg\ m^{-1}\ s^{-1}$). The permeability, k (m^2), depends only on the characteristics of the porous medium and will be used instead of K_s for the remainder of this study. The permeability can be expressed using Poiseulle's law as

$$k = \frac{R^2}{G} \tag{2}$$

where R (m^2) is a pore radius. The factor G is equal to 8 for circular tubes, but has other values for different pore shapes (e.g. Carman, 1939; Schlueter, 1995).

Poiseulle's law holds for straight cylindrical pores and as such cannot be applied directly to media having finite, tortuous, interconnected, and/or irregular pores of different sizes. Several of these complications are accounted for in the K–C equation (Carman, 1939), which is given by

$$k = \frac{\phi}{G\tau^2} 4R_{hv}^2 \tag{3}$$

where ϕ is the total pore volume and τ is the tortuosity given by the ratio of the microscopic and the macroscopic flow path. Central to the K–C equation is the concept of hydraulic radius of the void space, R_{hv}, which is defined as the pore volume divided by wetted area. In the case of full saturation, R_{hv} can be defined as the ratio of the porosity and the specific surface area, s (m^{-1})

$$R_{hv} = \phi/s \tag{4}$$

The hydraulic radius thus characterizes a porous medium with a conductive term, ϕ, and a frictional term, s. For a circular pore one finds $R = 2R_{hv}$, thus explaining the factor 4 in Eq. (3).

While the K–C equation allows the calculation of permeability of porous media having irregular pores, it is also subject to controversy. Dullien (1992, p 257) states that the K–C equation is only valid for media consisting of spherical particles of uniform size. Prediction of the permeability using Eq. (3) may thus strongly deviate from measurements for porous media having relatively broad particle size distributions. In addition, the approach assumes that the hydraulic radius represents the effective pore diameter of the medium. After considering a number of different pore geometries, Schlueter (1995) concluded that use of R_{hv} does not lead to systematic underprediction or overprediction of pore permeabilities. Hillel (1998, p 191), however, argues that the hydraulic radius may not be representative for media with bimodal pore size distributions, such as cracked clays. Pore connectivity is not addressed in the K–C equation since the equation in essence assumes that the porous medium has only circular pores of radius $2R_{hv}$. Dullien (1992, p 258) demonstrated that having two parallel pores of different radii yields higher permeabilities than inferred from the hydraulic radius. Conversely, serially connected pores with different radii yield lower permeabilities. It is therefore unlikely that the factors ϕ,R_{hv}, G, and τ^2 alone can adequately capture the permeability characteristics of all porous media.

The K–C equation is often not immediately applicable since G, τ^2, and s are generally not known. Dullien (1992, p 256) argued that τ^2 often serves as fudge factor that matches predicted to observed permeabilities and is often not independently observed. While s may be measured with gas adsorption or ethylene glycol monoethyl ether (EGME) methods, these methods also include nanometer size pore structures. From Eq. (2) it is clear that, as long as continuous micron-sized or larger pores are present, nanometer-sized pores are unlikely to affect flow on a

macroscopic scale. Hence, gas adsorption and EGME methods may yield hydraulic radii and permeabilities that are far too small.

The importance of the scale on which s and ϕ are determined was recognized by Berryman and Blair (1987). Using SEM microscopy on thin sections of sandstone, they showed that s and, to a lesser extent, ϕ increased with magnification. Using a similar methodology for soils, Lebron et al. (1999) showed that the hydraulic radius decreased substantially with increasing magnification. Berryman and Blair (1987) reasoned that pore-wall features smaller than about 1% of the radius of a characteristic pore size do not significantly affect flow. This in turn would impose a limit on the maximum magnification necessary for determining hydraulically relevant s from SEM images.

Two variants of the K–C equation have been proposed in attempts to lessen problems with surface area and tortuosity. Ahuja et al. (1984) used the concept of effective porosity, ϕ_e, which is that part of the porosity that contributes most to fluid flow. They defined the effective porosity as the total porosity minus the water content at -33 kPa. This approach thus incorporates only the larger pores with an equivalent capillary radius greater than 4.5 μm. Ahuja et al. (1984) further simplified the K–C equation by assuming that s and τ^2 varied with some power of ϕ_e, thus yielding the approximation

$$k = A\phi_e^B \tag{5}$$

where A and B are empirical constants that vary considerably with soil type (Ahuja et al., 1989; Messing, 1989).

A second variant of the K–C equation was proposed by Berryman and Blair (1987) and Blair et al. (1996) who incorporated a formation factor F

$$k = \frac{\phi^2}{cFs^2} = \frac{1}{cF}R_{hv}^2 \tag{6}$$

in which c is a geometry constant equal to 2 that results from the fact that G in Eq. (3) equals 8. The formation factor follows from the analogy between fluid flow and electrical current through a medium. It is defined as the ratio of the pore fluid electric conductivity and the bulk electric conductivity of a saturated porous medium (e.g. Bear, 1972, p 113) and can be related to tortuosity and porosity (e.g. Walsh and Brace, 1984)

$$F = \frac{\tau^2}{\phi} \tag{7}$$

To use the K–C definition given by Eq. (6), we still need to measure or approximate F. Adler et al. (1992) and Blair et al. (1996) estimated F using Archie's law, according to

$$F = \phi^{-m} \tag{8}$$

where m assumes values between 1.5 and 2 for sandstones, unconsolidated sand, and synthetic media (Blair et al., 1996; Bear, 1972, p 116).

The data obtained in this study allow us to evaluate the K–C variants given by Eqs. (5) and (6). In addition, we will generalize the K–C equation given in Eq. (3) by lumping the effects of all unknown factors (pore geometry, -tortuosity, -connectivity) and the constant 4 into one single parameter C

$$k = \frac{\phi_a^3}{Cs^2} = \frac{\phi_a}{C}R_{hv}^2 \tag{9}$$

where ϕ_a is an apparent porosity analogous to the effective porosity used in Eq. (5). Contrary to the parameter F in Eq. (6), which is interpreted in terms of porosity and tortuosity (cf. Eqs. (7) and (8)), the parameter C is free to be empirically related to various microscopic and macroscopic soil parameters.

2.2. Obtaining microscopic variables from SEM images

Two-point correlation functions are instrumental in this study for obtaining the surface area and other microscopic statistics of thin sections. Although we used SEM, the general principles outlined here can also be applied to images obtained with light microscopy.

Determination of a two-point correlation function requires a binary image, i.e. an image where the void and particle space are unequivocally defined. SEM images typically have a range of gray scale values owing to different atomic masses of the elements present in the thin sections. Gray values are normally bimodally distributed, such as depicted for two soils in Fig. 1. The left hand peak of soil 1 is caused by the hydrocarbon-based epoxy resin that fills the voids.

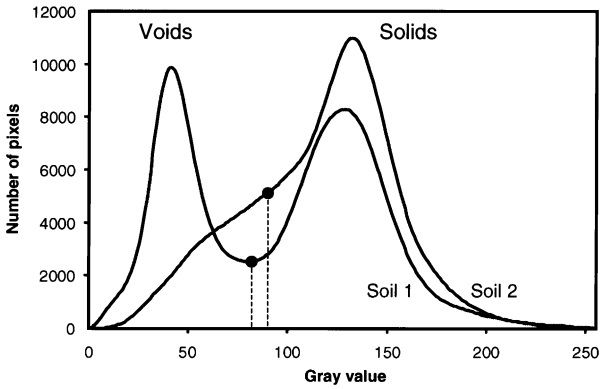

Fig. 1. Histograms of two SEM images. The position of the gray value thresholds is indicated with the dots. The graphs were passed through a low frequency bandpass filter to remove high frequency noise.

The right hand peak of soil 1 is caused by the particles containing heavier elements (Si, Ca, etc). By setting a threshold gray level, one can separate the pixels belonging to the void space from those belonging to the particles, thus yielding a binary SEM image.

Let $Z(x,y)$ represent a binary SEM image with $Z(x,y) = 1$ for pixels belonging to voids, and $Z(x,y) = 0$ for pixels belonging to particles. The integers x and y represent the horizontal and vertical coordinates of a pixel within the image according to $1 \le x \le x_{max}$ and $1 \le y \le y_{max}$, where x_{max} and y_{max} are the image sizes (1024 and 800 pixels, respectively). The apparent porosity, ϕ_a, of the SEM image is calculated as the average of $Z(x,y)$

$$\phi_a = \bar{Z}(x,y) \tag{10}$$

Due to the finite resolution of the images, the apparent porosity is usually smaller than the total porosity because pores smaller than the detection limit are not resolved.

Two-point correlation functions account for spatial structure in the images by considering each possible pixel pair (e.g. Berryman, 1985)

$$R_z(u,v) = \overline{Z(x,y)Z(x+u,y+v)} \tag{11}$$

where u and v are the lag distances in the x or y direction subject to the conditions: $0 \le u \le x_{max} - 1$, and $0 \le u \le y_{max} - 1$. The special case of a zero lag distance, $R_z(u=0, v=0)$, yields ϕ_a, since $Z(x,y)^2 = Z(x,y)$ for binary pixels (i.e. $1^2 = 1$ and $0^2 = 0$). For increasing lag distances the correlation decreases to $R_z(u,v) = \phi_a^2$ for completely uncorrelated pixels. By setting $Z(x,y) = 0$ for void pixels and $Z(x,y) = 1$ for particle pixels one can compute the correlation function of the particle space. While the definition of Eq. (11) is simple, its calculation is computer intensive. Appendix A explains how $R_z(u,v)$ may be computed quickly using Fast Fourier Transforms. Correlation functions may be easier to interpret visually when they are normalized according to (e.g. Quiblier, 1984)

$$R_{z,n}(u,v) = \frac{\overline{[Z(x,y) - \phi_a][Z(x+u,y+v) - \phi_a]}}{\phi_a - \phi_a^2} \tag{12}$$

which is equivalent to

$$R_{z,n}(u,v) = \frac{R_z(u,v) - \phi_a^2}{\phi_a - \phi_a^2} \tag{13}$$

In this case $R_{z,n}(u,v)$ is equal to one for $u = 0$ and $v = 0$, and equal to zero for uncorrelated distances.

The matrix $R_z(u,v)$ can be used to test the degree of isotropy of the SEM image by comparing the vectors $R_z(0,v)$ and $R_z(u,0)$. We found that our images were always sufficiently isotropic for the purposes of this study, and averaged $R_z(u,v)$ into a one-dimensional vector, $R_z(r)$, using a procedure outlined in Berryman (1985). The distance r is relative to $u = 0$ and $v = 0$, where $u = r\cos\gamma$ and $v = r\sin\gamma$; with γ representing the angle with the u axis.

The surface area, s (μm^{-1}), of the image can be derived from the slope of $R_z(r)$ by taking the limit

(Berryman and Blair, 1986)

$$\lim_{r\downarrow 0} \frac{dR_z(r)}{dr} = -s/4 \tag{14}$$

In this study we will compute s in a first order approximation

$$s = \frac{-4(R_z(1) - R_z(0))}{h} \tag{15}$$

where h is the resolution (pixel size in μm). Higher-order approaches do exist (e.g. Montemagno and Ma, 1999) that yield s that are usually substantially higher than those provided by Eq. (15). We did not use such higher order approaches because they provide s values that correspond more or less to higher resolutions; rather we believe that s and ϕ_a should be derived at the same scale.

Berryman and Blair (1987) established minimum and maximum bounds for s as follows

$$\frac{2}{h}\sqrt{\frac{\pi\phi_a}{x_{max}y_{max}}} \le s \le \frac{4\phi_a}{h} \tag{16}$$

Both bounds represent highly ordered arrangements of pixels that are unlikely to occur in soils. The minimum bound is obtained by concentrating all void pixels into *one* circular pore. This value turns out to be extremely small and represents the case where the sample displays the maximum amount of order. The maximum surface area is the case where all pixels are surrounded by voids, which requires an unrealistic checkerboard pattern for $\phi_a = 0.5$. We defined a more practical maximum surface area by considering a completely random arrangement of particle and void pixels. Pixels in this case have no correlation at any lag except zero and have the least amount of order. Therefore, the correlation will drop immediately from ϕ_a to ϕ_a^2 (cf. Eq. (11)). Following Eq. (15), the maximum surface area is then given by

$$s \le 4\frac{(\phi_a - \phi_a^2)}{h} \tag{17}$$

Following Eq. (4), the hydraulic radius void space, R_{hv}, is computed as

$$R_{hv} = \frac{\phi_a}{s} \tag{18}$$

Notice that we substituted ϕ_a for ϕ, and derived s from Eq. (15). To keep our approach consistent, we will use ϕ_a in all three K–C variants. We also point out that both ϕ_a and s, and therefore R_{hv}, depend on the magnification of the SEM images (cf. Berryman and Blair, 1987; Lebron et al., 1999). Ultimately, ϕ_a is bounded by ϕ, but s may increase much stronger with higher magnifications, resulting in smaller R_{hv}. The results in this study thus depend on the invoked magnification (50).

In analogy to the hydraulic radius for the void space, it is possible to characterize the particle space in a similar fashion. Because the surface areas of the void and particle spaces are the same, the 'hydraulic radius' of the particle space, R_{hs}, should be

$$R_{hs} = \frac{1 - \phi_a}{s} \tag{19}$$

Coincidently, the ratio of R_{hv} and R_{hs} yields a relative measure of the pore and particle sizes that is dependent only on ϕ_a

$$\beta = \frac{R_{hv}}{R_{hs}} = \frac{\phi_a}{1 - \phi_a} \tag{20}$$

This ratio is reminiscent of the void ratio used by Arya and Paris (1981) and similar to a packing parameter used by Haverkamp and Parlange (1986). These two studies, however, focused on water retention rather than hydraulic conductivity and used the total porosity instead of an apparent porosity.

Berryman and Blair (1987) proposed a characteristic pore size, R_c, defined as the intersection of the tangent of the correlation function at lag 0 and the horizontal line given by ϕ_a^2

$$R_c = \frac{4(\phi_a - \phi_a^2)}{s} = 4R_{hv}(1 - \phi_a) = 4R_{hs}\phi_a \tag{21}$$

It follows that R_c is identical for the void and solid spaces, and strongly related to the hydraulic radii.

Eqs. (18)–(21) provide information about characteristics of the porous medium derived from lag 0 and 1 in the correlation function, $R_z(r)$ (cf. Eqs. (10) and 15). Correlations at greater lag distances may also influence C because they provide information about larger-scale soil structure. Long-range information in $R_z(r)$ may be derived from the distance where correlation in $R_z(r)$ is no longer present (i.e. $R_z(r) = \phi_a^2$ or $R_{z,n}(r) = 0$). Because $R_{z,n}(r)$ did not always reach 0 but remained at a very small positive value, we

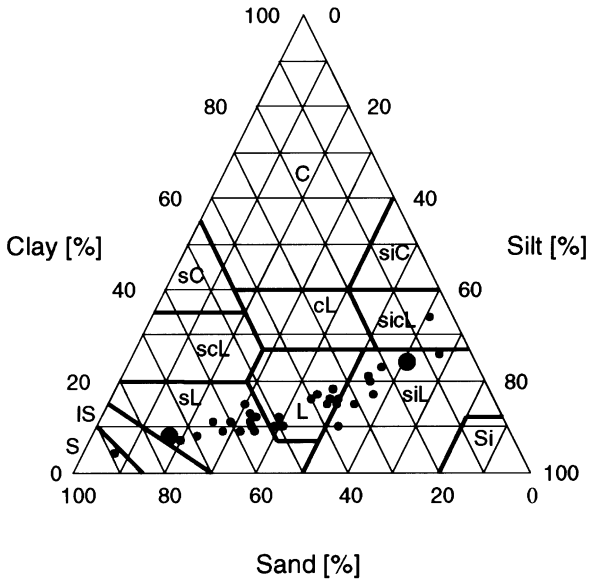

Fig. 2. Textural distribution of the 35 soils used in this study (USDA classification). The large dots depict the two samples in Fig. 3. S: sand, lS: loamy sand, sL: sandy loam, scL: sandy clay loam, sC: sandy clay, L: loam, siL: silty loam, Si: silt, sicL: silty clay loam, siC: silty clay, cL: clay loam, C: clay.

defined the characteristic long range distance variable R_L as the distance where $R_{z,n}(r)$ first reached 0.02.

3. Materials and methods

3.1. Samples

We obtained 36 undisturbed Gila silt loam soil samples from an irrigated field in Coachella Valley, California. The samples were collected from the topsoil and were 12 cm long and 12 cm in diameter. The saturated hydraulic conductivity (K_s) was measured with the constant head method using water having the same chemical composition as used for irrigation of the field. The measurements were repeated until a constant K_s was found for each sample. In order to compute k from K_s (Eq. (1)) we used $g = 9.81\ \mathrm{m\ s^{-2}}$, $\rho = 998\ \mathrm{kg\ m^{-1}}$, and $\eta = 1.002 \times 10^{-3}\ \mathrm{kg\ m^{-1}\ s^{-1}}$.

After determination of the bulk density, the cores were split vertically. One half was used for determining the particle size distribution (given in Fig. 2) and the particle density. The other half was used to prepare thin sections by impregnating the soil with epoxy (EPO-TEK 301, Epoxy technology, Billerica, MA)[1]. A horizontally oriented 3.5×2.5 cm section was cut from the hardened sample (i.e. the section was perpendicular to the water flow direction during the K_s measurements) and mounted on a glass slide. A thin section of approximately 35 μm thickness was subsequently prepared using diamond polishers, thereby avoiding chemical contamination. We did not cover the thin sections with glass plates since this would interfere with the SEM measurements.

3.2. SEM technique

An AMRAY 3200 (AMRAY Inc., Bedford, MA) scanning electron microscope with a backscatter electron detector was used to obtain images of the thin sections. This technique requires no metal coating of the samples because the low vacuum ensures the removal of surface charge buildup. Images were obtained at a magnification of 50 and a resolution of 1024×800 pixels with a 16-bit numerical resolution. The magnification was chosen to obtain a reasonable

[1] Trade names are provided for the benefit of the reader and do not imply endorsement by the USDA.

sample area for which the correlation functions were expected to capture most or all relevant spatial information. The corresponding resolution was 1.88 μm pixel^{-1}, which is better than the 7 μm obtained by Lebron et al. (1999) who used commercial image analysis software. The capillary law shows that the resolution adequately resolved pores with radii of 4.5 μm that correspond to the effective porosity at 33 kPa (Ahuja et al., 1984). Each image covered an area of approximately 2.9 mm^2. We retrieved 10 images from most thin sections; on a few occasions instrumental difficulties limited this number, resulting in 340 images for 36 samples totaling 600 MB of data.

3.3. Selection of threshold gray value

Histograms of the images were compiled by sorting the gray values in 256 classes as demonstrated in Fig. 1 for two soils. The left hand peak of soil 1 is caused by the epoxy resin (pore space), while the right hand peak represents the particle space. The minimum between the peaks indicates the position of a threshold gray value (method 1). The peaks are not well resolved for soil 2, which makes the identification of a threshold value more difficult. In this case we determined the threshold using the inflection point of the histogram (method 2). We obtained 265 thresholds with method 1 and 55 with method 2. Twenty images and one sample were not considered for further analyses because of erratic histograms or underexposures. This resulted in 35 samples and 320 images for further analyses.

3.4. Method of data analysis

The Ahuja and Berryman variants of the K–C equation (Eq. (5) and (6), respectively) were fitted directly to the measured permeabilities. This yielded estimates of the parameters A and B in Ahuja's model, and the parameter m in Berryman's model (Eq. (8)). The optimizations were performed on log k data to avoid a bias towards samples with high permeabilities. The model results were evaluated with coefficients of determination (R^2) and root mean square errors (RMSE), the latter given by

$$RMSE = \sqrt{\sum(\log k - \log k')^2/N} \tag{22}$$

where N is the number of samples (35) and k and k' are the measured and predicted permeabilities, respectively. Because we used logarithms of k, the RMSE values have no units. The R^2 and RMSE values were calculated for permeabilities based on average ϕ_a (Ahuja model) or R_{hv} (Berryman and general models) for each thin section. Error propagation rules allowed us to assign error bars for individual predictions of k using standard deviations computed for ϕ_a and R_{hv} for each thin section.

In the case of the general K–C equation (Eq. (9)), we first needed estimates of C before this parameter could be correlated to microscopic and macroscopic data. To this end, we computed log C for each sample from the difference between the logarithms of predicted and measured permeabilities (cf. Eq. (9)) according to

$$\log C = \log(\phi_a R_{hv}^2) - \log k \tag{23}$$

To investigate the correlation structure between log C and other variables we first computed a Spearman rank correlation matrix. Spearman rank correlations were chosen over linear correlations to allow for the possibility of non-normal distributions. The correlation matrix was subsequently used to identify potential macroscopic and microscopic predictors of C. Macroscopic predictors consisted of percentages sand, silt, and clay, bulk density (BD), particle density (ρ_s), and porosity (ϕ), the latter was computed as: $\phi = 1 - BD/\rho_s$. Potential microscopic predictors of C included ϕ_a, s, R_{hv}, R_{hs}, R_c, R_L, and β.

Three different strategies were tested to predict C: macroscopic data only, microscopic data only, and a combination of both. Predictions of C were obtained using a combination of artificial neural networks (ANN) and the bootstrap method. Artificial neural networks were chosen because they excel in finding patterns in multivariate data. The bootstrap method (Efron and Tibshirani, 1993) was used to estimate the uncertainty in predicted C. Combining neural networks with the bootstrap method also avoided overfitting problems (cf. Haykin, 1994 p 176) that may occur in small data sets such as those used in our study. We refer to Schaap and Leij (1998) and Schaap et al. (1999) for more elaborate descriptions of ANNs and the bootstrap method.

In terms of practical applicability it is preferable to predict ϕ_a, and s from easily measurable macroscopic

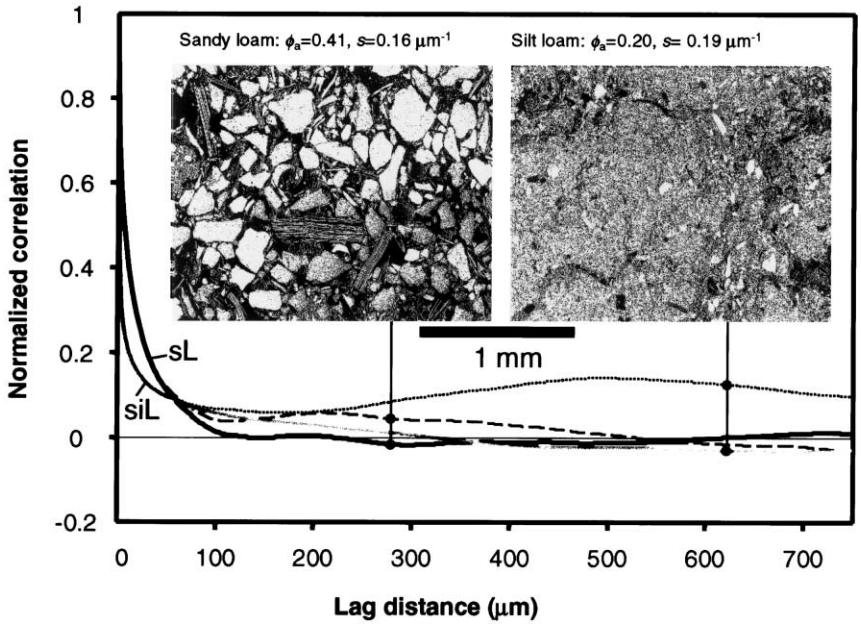

Fig. 3. Examples of SEM images and corresponding correlation functions for a sandy loam (sL) and a silt loam (siL). The solid curves give the correlation functions for the void space, the dashed lines provide the correlations for the particle space. The apparent porosity (ϕ_a) and specific surface (s) area are also listed.

variables instead of measuring them with SEM. We therefore developed models that predicted these parameters, as well as C, from macroscopic variables. The resulting models still assume that the physical background of the K–C relation is valid (Eq. (9)). We will compare these models with a fully empirical version that predicts k directly from macroscopic parameters without first predicting C, ϕ_a, and s.

4. Results

4.1. Correlation functions, apparent porosity and surface area

Fig. 3 gives typical examples of the normalized correlation functions (Eq. (13)) for void and particle space for a sandy loam and a silt loam (indicated by the large dots in Fig. 2). The images corresponding to these correlation functions are also shown. The apparent porosities were different (0.41 and 0.20 for the sandy loam and silt loam, respectively). However, the surface area's were similar (0.16 vs. 0.19 μm^{-1}). The small difference is probably related to the low porosity of the silt loam, which left its small pores unresolved. The resulting hydraulic radii were 2.61 and 1.04 μm for the sandy loam and silt loam, respectively. Up until a distance of 60 μm, the correlations for the void (solid line) and particle spaces (dashed lines) of the sandy loam were higher than those for the silt loam. The correlation function for the void space of the sandy loam reached zero at 150 μm, while the silt loam reached zero correlation at 330 μm. The particle and void correlation functions closely resembled each other between 0 and 60 μm but diverged after this distance. The correlation function for the particle space of the sandy loam remained positive until 550 μm, whereas the correlation for the silt loam did not reach a zero correlation within 750 μm. Note that the correlations of the void space were not exactly zero at longer distances, but alternated between small negative and positive values. These and similar findings in other images indicate that both particle and void space exhibit long range correlation structures which are probably due to aggregation of soil particles and simultaneous exclusion of larger pores. However, results for the long-range correlation distance (R_L) for pore and

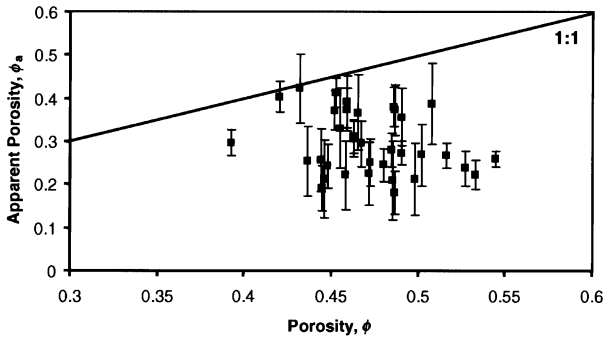

Fig. 4. Distribution of the apparent porosity (ϕ_a) versus measured porosity (ϕ). The error bars denote one standard deviation.

particle space varied strongly among images from the same thin section. This casts doubt that R_L can provide useful information about the long-range structure of the void or particle space. We tried several other approaches to characterize the long-range structure, but were unsuccessful thus far.

Fig. 4 shows that ϕ_a was always smaller than the total porosity. No significant correlation was found between ϕ_a and ϕ (see also Table 1). Because no large (millimeter sized) pores were present in our samples, these data suggest that a relatively large amount of pore volume is locked up in pores smaller than the detection limit (1.88 μm). The error bars in Fig. 4 denote one standard deviation errors and indicate that thin sections of some samples had a considerable variation in ϕ_a. The average standard error of ϕ_a was 0.020 $cm^3\,cm^{-3}$, the average coefficient of variation was 7.4%.

Fig. 5 shows a plot of the surface area, s, versus apparent porosity, ϕ_a, for all 320 SEM images. The average surface areas for each sample are indicated with the squares and corresponding error bars (one standard deviation). All samples had surface areas smaller than the maximum given by Eq. (17) as depicted by their position under the parabola. This indicates that the void pixels had a considerable amount of order. The images with the smallest ϕ_a had positions closest to the parabola and thus have the highest degree of 'randomness' in pixel distribution (cf. Eq. (17)). There was an almost linear increase in surface area until $\phi_a = 0.3$, suggesting a more or less constant hydraulic radius (Eq. (18)). Beyond $\phi_a = 0.3$ the surface area appears to decrease, resulting in larger hydraulic radii and increased order. It is presently unknown whether the maximum at $\phi_a = 0.3$ is a characteristic of the studied soil series or reflects the fact that higher porosities require more order to keep the pore-particle structure stable. The standard error in s was 0.013 m^{-1}, while the average coefficient of variation was 6.5%.

4.2. Evaluation of Kozeny–Carman models

Optimization of the Ahuja model (Eq. (5)) to measured $\log k$ yielded $\log(A) = -11.185$ and $B = 4.231$ with a coefficient of determination (R^2) of 0.36 and an RMSE of 0.58 m^2 (Table 2). When we used total porosity instead of apparent porosity, we obtained an R^2 of 0.13. Fig. 6 shows predictions of

Table 1
Spearman rank correlations between parameters in the K–C equations (horizontal) and potential macroscopic and microscopic predictors of these parameters (vertical). The numbers in italics denote significant correlations (at $\rho < 0.05$)

	ϕ_a	s	R_{hv}	k	F	C
Clay	*−0.49*	*0.63*	*−0.73*	*−0.84*	*0.71*	*0.65*
Silt	*−0.45*	*0.62*	*−0.70*	*−0.67*	*0.52*	*0.47*
Sand	*0.46*	*−0.66*	*0.72*	*0.71*	*−0.58*	*−0.53*
Bulk d.	0.02	−0.27	0.17	0.10	−0.06	−0.09
ρ_s	*−0.42*	*0.44*	*−0.55*	*−0.58*	*0.42*	*0.34*
ϕ	−0.21	*0.46*	*−0.42*	*−0.35*	0.20	0.20
ϕ_a	1.00	−0.21	*0.79*	*0.65*	*−0.35*	−0.12
s	−0.21	1.00	*−0.72*	*−0.60*	*0.38*	*0.34*
R_{hv}	*0.79*	*−0.72*	1.00	*0.80*	*−0.47*	−0.31
R_{hs}	−0.18	*−0.89*	*0.39*	*0.35*	−0.26	−0.32
R_c	*0.68*	*−0.82*	*0.98*	*0.80*	*−0.50*	*−0.35*
R_l	−0.04	−0.04	0.04	0.00	0.05	0.02
β	*1.00*	−0.21	*0.79*	*0.65*	*−0.35*	0.12

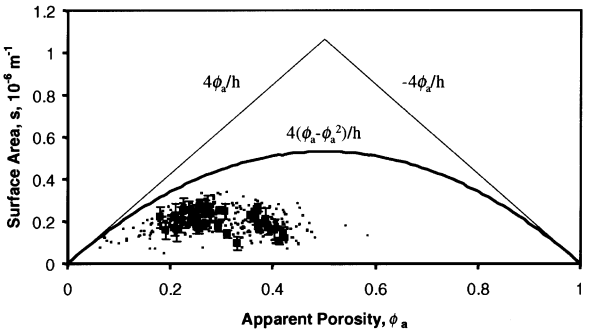

Fig. 5. Distribution of the surface area (s) versus apparent porosity (ϕ_a). The dots denote the surface area for each individual SEM image. The squares represent the average surface area for each sample (with one standard deviation error bars). The triangle represents the maximum possible surface area according to Eq. (16), while the parabola denoted the maximum surface area according to Eq. (17).

log k versus measured log k values as well as the one standard deviation error bars of the predictions. Although the Ahuja model may work well for some soils (Messing, 1989; Ahuja et al., 1989; Schaap et al., 1998), our results with this model are not as good as those obtained with the other K–C variants, as will be discussed later. Reasons for this may be the assumption that tortuosity and surface area should decrease with some power of ϕ_a (Ahuja et al., 1989). While we could not retrieve any direct information about the tortuosity from our data, we notice from Fig. 5 that a more complex relationship between s and ϕ_a may be present.

For the Berryman model we obtained $m = 2.76$

Table 2
Results for the three K–C model variants. The Ahuja and Berryman models are listed with all their input data, the input data for the general model only pertain to C. In addition, measured ϕ_a and s are needed for this model. The RMSE values have no units because logarithmic values were used

	Input	log(C)		log(k)	
		R^2	RMSE	R^2	RMSE
Ahuja	ϕ_a	–	–	0.36	0.58
Berryman	ϕ_a, s	–	–	0.57	0.48
General Model					
Macroscopic input	Silt, Clay	0.61	0.29	0.85	0.28
	Silt, Clay, BD	0.71	0.26	0.87	0.25
	Silt, Clay, ρ_s	0.71	0.26	0.88	0.25
	Silt, Clay, ϕ	0.68	0.27	0.87	0.26
Microscopic input	s, R_c	0.30	0.40	0.71	0.40
	S	0.24	0.40	0.69	0.40
	ϕ_a	0.12	0.43	0.65	0.43
	R_c	0.21	0.41	0.68	0.41
	ϕ_a, s	0.33	0.38	0.72	0.38
Microscopic and macrocopic input	Silt, Clay, s	0.64	0.28	0.85	0.28
	Silt, Clay,R_c	0.67	0.26	0.87	0.26
	Silt, Clay, ρ_s, s	0.71	0.26	0.88	0.25
	Silt, Clay, ρ_s, R_c	0.77	0.24	0.90	0.24
	Silt, Clay, ρ_s, ϕ_a, s	0.81	0.23	0.91	0.23

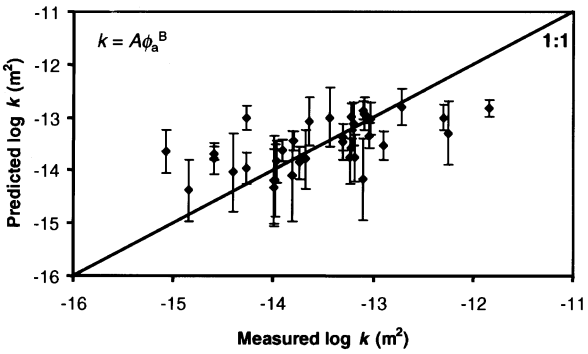

Fig. 6. Predictions of permeability by the Ahuja model (Eq. (5)) with one standard deviation errorbars.

with a corresponding R^2 of 0.57 and an RMSE of 0.48 m^2 (Table 2). Fig. 7 shows predictions of log k are plotted versus measured log k values in Fig. 7 as well as one standard deviation error bars of the predictions. The value for m was found to be considerably higher than those reported by Blair et al. (1996) who listed F values that correspond to m values between 1.5 and 2. The data of Blair et al. (1996), however, pertain to sandstones, not soils with a wide range of textures. When the formation factor, F, is interpreted in terms of Eq. (7) we obtain tortuosities between 1.24 and 12.7. While the lower value is reasonable, we strongly doubt that the higher value can be solely attributed to tortuosity. The formation factor F is most likely influenced by other factors as well, such as pore geometry and connectivity. Table 1 shows that F exhibits only a weak Spearman rank correlation (−0.35) with apparent porosity (cf. Eq. (7)) but a much stronger correlation with texture, especially clay content (0.71).

In the case of the general model (Eq. (9)), we first computed log C according to Eq. (23). Subsequently, we computed the Spearman rank correlations between C and macroscopic and microscopic variables. Notice that C had smaller absolute rank correlations than k for all the variables listed in Table 2. These reduced correlations were to be expected because the term $\phi_a R_{hv}^2$ in Eq. (9) accounts for the K–C concepts such as hydraulic radius and effective pore volume while C accounts for the remaining media properties such as tortuosity and connectivity. The strongest correlations were found for texture, while minor correlations were present for solid density, specific surface area and the characteristic pore length R_c. No significant relations were found for bulk density, total porosity, the hydraulic radii R_{hs} and R_{hv}, the long-range radius R_L, and the void ratio β.

Table 2 presents results of the ANN-bootstrap analyses to predict C from the most promising predictors in Table 1. When log C was predicted from

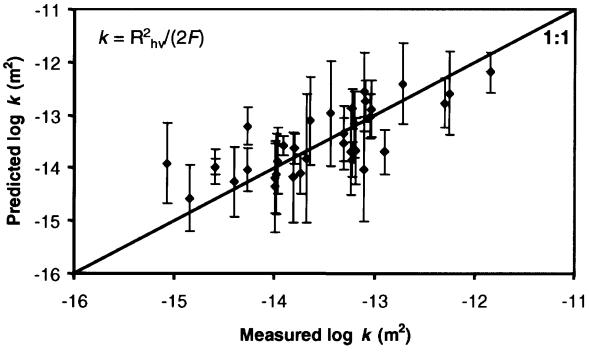

Fig. 7. Predictions of permeability by the Berryman model (Eq. (6)) with one standard deviation errorbars.

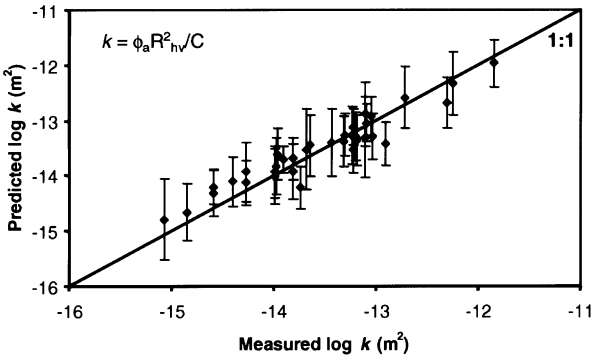

Fig. 8. Predictions of permeability by the general model (Eq. (9)) using silt, clay, ρ_s, ϕ_a, and s as input (Table 2). The error bars denote one standard deviation.

macroscopic variables, R^2 values between 0.61 and 0.68 were obtained, which in turn led to R^2 between 0.85 and 0.88 for log k. The textural variables provided the most information, while bulk density, particle density, or porosity increased the correlations slightly. Models that used only microscopic variables all showed poor correlations with log C as was already clear from Table 1. The corresponding R^2 for log k ranged between 0.65 and 0.72. A combination of macroscopic and microscopic variables increased the R^2 for log k to the 0.85–0.91 range, while corresponding RMSE values were slightly higher than those of the macroscopic models. The best model used silt and clay percentages, particle density, ϕ_a, and s as input. This model is displayed in Fig. 8, which also shows the error bars generated with the bootstrap method. However, we believe that not too much physical meaning should be attributed to the superiority of this model with respect to other macroscopic variants because unknown systematic or random errors in the small data set (35 samples) may have provoked statistical artifacts.

Table 3 shows results of the model that predicted C, as well as ϕ_a, and s from macroscopic variables. In comparison with macroscopic results in Table 2, the results are quite good. For example, the macroscopic model in Table 2 that used clay, silt and ρ_s to predict C, but used measured ϕ_a, and s values, yielded an R^2 of 0.88 for log k and an RMSE of 0.25. The macroscopic model in Table 3 that used the same input data to predict C, ϕ_a, and s, yielded an R^2 of 0.87 and an RMSE of 0.29. Texture (silt and clay percentages) was the main factor that contributed to the prediction of ϕ_a, s and C. Bulk density, ρ_s, and ϕ contributed only little, if any, information. These results indicate that, ϕ_a, s and C can be estimated from macroscopic variables without greatly deteriorating the predictions of k.

Table 3
Results Eq. (9) using predicted ϕ_a, s, and C to predict k (general model) and results for the direct prediction of k (fully empirical model)

	Input	ϕ_a		s		log(C)		log(k)	
		R^2	RMSE	R^2	RMSE	R^2	RMSE	R^2	RMSE
General Model	Silt, Clay	0.38	0.056	0.61	0.029	0.62	0.29	0.81	0.32
	Silt, Clay, BD	0.41	0.056	0.61	0.029	0.66	0.28	0.85	0.31
	Silt, Clay, ρ_s	0.49	0.053	0.62	0.029	0.69	0.26	0.87	0.29
	Silt, Clay, ϕ	0.39	0.056	0.59	0.029	0.64	0.28	0.84	0.31
Fully empirical model	Silt, Clay	–	–	–	–	–	–	0.81	0.32
	Silt, Clay, BD	–	–	–	–	–	–	0.83	0.30
	Silt, Clay, ρ_s	–	–	–	–	–	–	0.84	0.32
	Silt, Clay, ϕ	–	–	–	–	–	–	0.80	0.33

A fully empirical prediction of k (i.e. by a model that predicts $\log k$ directly and does not use K–C concepts), yielded an R^2 of 0.84 and an RMSE of 0.32. These results indicate that models that impose physical constraints on relationships among variables perform equal or better than fully empirical models that are not subject to such constraints. The results of the fully empirical model further provide indirect evidence of the validity of the K–C approach because such a model would probably have shown better results if the K–C approach were invalid. The transparency of predictions of permeability may thus be greatly enhanced by using K–C concepts supplemented by a textural or soil dependent factor C and estimated ϕ_a, s.

5. Summary and conclusions

In this study we used porosities and surface area's derived from SEM images of thin sections to test three Kozeny–Carman models for prediction of the permeability. We found that the simplifications made by Ahuja et al. (1984) and Berryman and Blair (1987) were not as effective in predicting k as a more general approach that lumped the effects of pore tortuosity, connectivity and geometry into one empirical parameter, C. We showed that C is predominantly related to texture and leads to better predictions of k with R^2 values between 0.85 and 0.91, depending upon inclusion of additional predictors. This model still used surface area and apparent porosity that need to be derived from thin sections. We showed that the microscopic surface area and apparent porosity could be predicted from texture, leading to an only slightly reduced model effectiveness. While this model required only macroscopic data to predict permeability in a semi physical way, development of this model would not have been possible without microscopic information. A completely empirical model that predicted the permeability directly did not yield better results, indicating that the general K–C model makes efficient use of the available information.

Our current data set was relatively small and limited to only one series of homogeneous soils. More measurements of ϕ_a, s, and other microscopic variables are needed in order to cover a wider range of soils and expand the models towards general applicability. Furthermore, our study was limited to only one magnification (50); additional measurements involving other magnifications may yield more information about possible relationships among microscopic and macroscopic variables. Some scale issues may also need to be resolved because, unlike the soils in this study, many soils are inhomogeneous and may exhibit structure that extends beyond the scale that we were able to observe with SEM. It should be interesting to expand our current work to include water retention and the unsaturated hydraulic conductivity.

Acknowledgements

The authors gratefully acknowledge the support by NSF and NASA (grants EAR-9804902 and EAR-0074841).

Appendix A

Although the formulation of $R_z(u, v)$ (Eq. (11)) is relatively simple, its calculation requires more than 10^{10} multiplications for images in the order of 10^6 pixels. The computation time can be reduced from hours to minutes (on Pentium PC's) by carrying out the correlation in the frequency domain using two-dimensional Fast Fourier Transforms (Berryman, 1985; Press et al., 1988). In order for the correlation to work properly, it is necessary to perform the transform on an image that is twice the size in both the x and y directions using 'zero padding' (cf. Press et al., 1988). Also, the Fast Fourier Transform will only work correctly on x_{max} and y_{max} that are powers of two (Press et al., 1988). We therefore expanded the binary version of the original 1024×800 pixel image to 2048×2048 pixels by adding zeros. Total computer memory requirements were approximately 32 MB of RAM. Representations of $Z(x,y)$ in the frequency domain were obtained with a two-dimensional Fast Fourier Transform

$$Z_f(f_x,f_y) = \mathrm{FFT}_2[Z(x, y)] \tag{A1}$$

where f_x and f_y are the frequencies in the x and y directions, respectively. Subsequently, Z_f was

multiplied with its complex conjugate Z_f^* for each f_x and f_y

$$C_z(f_x,f_y) = Z_f(f_x,f_y)Z_f^*(f_x,f_y) \quad \text{(A2)}$$

The correlation matrix $R_z(u,v)$ then follows from the inverse Fourier transform

$$R_z(u,v) = \frac{\text{IFFT}_2[C(f_x,f_y)]}{(x_{max}-u)(y_{max}-v)} \quad \text{(A3)}$$

where the denominator represents a normalization for the number of points pertaining to a particular combination of u and v.

References

Adler, P.M., Jacquin, C.G., Thovert, J-F., 1992. The formation factor of reconstructed porous media. Water Resour. Res. 28 (6), 1571–1576.

Ahuja, L.R., Naney, J.W., Green, R.E., Nielsen, D.R., 1984. Macroporosity to characterize spatial variability of hydraulic conductivity and effects of land management. Soil Sci. Soc. Am. J. 48, 699–702.

Ahuja, L.R., Cassel, D.K., Bruce, R.R., Barnes, B.B., 1989. Evaluation of spatial distribution of hydraulic conductivity using effective porosity data. Soil Sci. 148, 404–411.

Arya, L.M., Paris, J.F., 1981. A physico-empirical model to predict the soil moisture characteristic from particle-size distribution and bulk density data. Soil Sci. Soc. Am. J. 45, 1023–1030.

Arya, L.M., Leij, F.J., van Genuchten, M.Th., Shouse, P.J., 1999a. Scaling parameter to predict the soil water characteristic from particle-size distribution data. Soil Sci. Soc. Am. J. 63, 510–519.

Arya, L.M., Leij, F.J., Shouse, P.J., 1999b. Relationship between the hydraulic conductivity function and the particle-size distribution. Soil Sci. Soc. Am. J. 63, 1063–1070.

Bear, J., 1972. Dynamics of fluids in porous media. American Elsevier, New York 764 p..

Berryman, J.G., 1985. Measurement of spatial correlation functions using image processing techniques. J. Appl. Phys. 57 (7), 2374–2384.

Berryman, J.G., Blair, S.C., 1986. Use of digital image analysis to estimate fluid permeability of porous materials:Application of two-point correlation functions. J. Appl. Phys. 60 (6), 1930–1938.

Berryman, J.G., Blair, S.C., 1987. Kozeny-Carman relations and image processing methods for estimating Darcy's constant. J. Appl. Phys. 62 (6), 2221–2228.

Blair, S.C., Berge, P.A., Berryman, J.G., 1996. Using two-point correlation functions to characterize microgeometry and estimate permeabilities of sandstones and porous glass. J. Geophys. Res. 101 (B9), 20,359–20,375.

Bouma, J., Jongerius, A., Schoonderbeek, D., 1979. Calculation of saturated hydraulic conductivity of some pedal clay soils using micromorphometric data. Soil Sci. Soc. Am. J. 43, 261–264.

Carman, P.C., 1939. Permeability of saturated sands soils and clays. J. Agric. Sci. 29, 262–273.

Dullien, F.A.L., 1992. Porous Media: Fluid Transport and Pore Structure. . 2nd edAcademic Press, San Diego 574 p..

Efron, B., Tibshirani, R.J., 1993. An Introduction to the Bootstrap. Monographs on Statistics and Applied Probability. Chapman and Hall, New York.

Haverkamp, R., Parlange, J.Y., 1986. Predicting the water-retention curve from particle size distribution. 1. Sandy soils without organic matter. Soil Sci. 142, 325–339.

Haykin, S., 1994. Neural Networks, A Comprehensive Foundation. . 1st edMacmillan College Publishing Company, New York 696 p..

Hillel, D., 1998. Environmental Soil Physics. Academic Press, San Diego 771 p..

Lebron, I., Schaap, M.G., Suarez, D.L., 1999. Saturated hydraulic conductivity prediction from microscopic pore geometry measurements and neural network analysis. Water Resour. Res. 35, 3149–3158.

Messing, I., 1989. Estimation of the saturated hydraulic conductivity in clay soils from soil moisture retention data. Soil Sci. Am. J. 53, 665–668.

Montemagno, C.D., Ma, Y., 1999. Measurement of interfacial surface areas for two-phase flow in porous media from PVI data. In: van Genuchten, M.Th., Leij, F.J., Wu, L. (Eds.). Proceedings of the International Workshop, Characterization and Measurements of the Hydraulic Properties of Unsaturated Porous Media. University of California Press, Riverside, pp. 121–132.

Mualem, Y., 1976. A new model predicting the hydraulic conductivity of unsaturated porous media. Water Resour. Res. 12, 513–522.

Or, D., Tuller, M., 1999. Liquid retention and interfacial area in variably saturated porous media: upscaling from single-pore to sample scale model. Water Resour. Res. 35, 3591–3605.

Or, D., Tuller, M., 2000. Flow in unsaturated fractured porous media: hydraulic conductivity of rough surfaces. Water Resour. Res. 36, 1165–1177.

Press, W.H., Flannery, B.P., Teukolsky, S.A., Vetterling, W.T., 1988. Numerical Recipes in C. . 1st edCambridge University Press, New York.

Quiblier, J.A., 1984. A new three-dimensional modeling technique for studying porous media. J. Colloid Interface Sci. 98, 84–102.

Schaap, M.G., Leij, F.J., 1998. Database related accuracy and uncertainty of pedotransfer functions. Soil Sci. 163, 765–779.

Schaap, M.G., Leij, F.J., van Genuchten, M.Th., 1998. Neural network analysis for Hierachical prediction of soil hydraulic properties. Soil Sci. Soc. Am. J. 62, 847–855.

Schaap, M.G., Leij, F.J., van Genuchten, M.Th., 1999. A bootstrap-neural network approach to predict soil hydraulic parameters. In: van Genuchten, M.Th., Leij, F.J., Wu, L. (Eds.). Proceedings of the International Workshop, Characterization and Measurements of the Hydraulic Properties of Unsaturated Porous Media. University of California Press, Riverside, pp. 1237–1250.

Schlueter, E.M., 1995. Predicting the transport properties of sedimentary rochs from microstructure. Ph.D. thesis, Lawrence Berkely Laboratory/University of California, Berkely, Berkely, California.

Tuller, M., Or, D., Dudley, L.M., 1999. Adsorption and capillary condensation in porous media: liquid retention and interfacial configurations in angular pores. Water Resour. Res. 35, 1949–1964.

Vogel, H.J., 1997. Morphological determination of pore connectivity as a function of pore size using serial sections. Eur. J. Soil Sci. 48, 365–377.

Vogel, H.J., Roth, K., 1998. A new approach for determining effective soil hydraulic functions. Eur. J. Soil Sci. 49, 547–556.

Walsh, J.B., Brace, W.F., 1984. The effect of pressure on porosity and the transport properties of rock. J. Geophys. Res. 89 (B11), 9425–9431.